



Twin-brush ZnO mesocrystal for the piezo-activation of peroxymonosulfate to remove ibuprofen in water: Performance and mechanism

Minxian Zhang^a, Hengcong Tao^b, Chunyang Zhai^{c,*}, Jingling Yang^{a,d,**}, Yingtang Zhou^b, Dehua Xia^d, Gabriele Comodi^e, Mingshan Zhu^{a,*}

^a Guangdong Key Laboratory of Environmental Pollution and Health, School of Environment, Jinan University, Guangzhou 511443, PR China

^b School of Petrochemical Engineering & Environment, Zhejiang Ocean University, Zhoushan 316022, PR China

^c School of Materials Science and Chemical Engineering, Ningbo University, Ningbo 315000, PR China

^d Guangdong Provincial Key Laboratory of Environmental Pollution Control and Remediation Technology, Sun Yat-sen University, Guangzhou 510275, PR China

^e Department of Industrial Engineering and Mathematical Sciences, Università Politecnica delle Marche, Via Brecce Bianche, 60131 Ancona, Italy

ARTICLE INFO

Keywords:

Peroxymonosulfate
Utilization efficiency
ZnO mesocrystal
Piezo-activation
Ibuprofen removal

ABSTRACT

Mesocrystals are highly ordered mesoporous superstructures with rich defects and high internal porosity, which are featured by the anisotropic charge migration in catalysis. In this work, we first used twin-brush hierarchical structures of ZnO (TB-ZnO) as piezoelectric mesocrystal with abundant oxygen vacancies to activate peroxymonosulfate (PMS) under piezoelectric activation. Compared with non-mesocrystal of common ZnO nanorods (NR-ZnO), TB-ZnO exhibited 3.7 times of performance for the ibuprofen (IBP) pollutants degradation in the presence of PMS and ultrasonic vibration, and achieved a high PMS utilization efficiency that exceeds the state-of-the-art catalysts. Experimental and theoretical results revealed that the presence of oxygen vacancies together with order mesoporous superstructures in TB-ZnO promoted the electron transfer, decreased the reaction barriers, and facilitated the mass transfer, thus enabling more electrons to participate in PMS activation. These findings open up an avenue to improving the utilization efficiency of PMS in the piezo-activation system for environmental remediation.

1. Introduction

Peroxymonosulfate (PMS)-based advanced oxidation processes (AOPs) have recently attracted much attention in water treatment [1,2]. Numerous techniques were reported to motivate PMS to yield radical or nonradical reactive species for organic pollutants degradation in wastewater [3–5]. However, the state-of-the-art PMS-based AOPs systems still suffer from unsatisfactory PMS utilization efficiency despite the high PMS consumption in most PMS-based AOPs systems [6–11]. The unsatisfactory PMS utilization efficiency is a critical factor that constrains the application of PMS-based AOPs, which is directly related to the catalytic efficiency and operating costs. The enhanced PMS utilization efficiency could in turn result in generating more reactive species to facilitate the catalytic reactions, and also decrease the amount of residual PMS to increase the environmental friendliness of process, while reducing PMS cost. Therefore, it is necessary to develop a

cost-effective and eco-friendly PMS activation system with high rate of PMS activation and utilization.

Recently, piezoelectricity, as a physical phenomenon mediated by transformation from mechanical energy to polarization charges, has been broadly applied in the degradation of various organic pollutants [12–19]. Taking advantage of these piezoelectric polarization charges, the O–O bond of PMS can be cleaved to form various reactive oxygen species (ROS, e.g., $\text{SO}_4^{\bullet-}$, HO^{\bullet} , $\text{O}_2^{\bullet-}$ and $^1\text{O}_2$). For example, our group first used BaTiO_3 as the piezoelectric material to activate PMS for benzothiazole pollutants degradation [20]. Compared with traditional UV (313 nm) and thermal (60 °C) activation methods, the reaction rate constant of piezo-activation PMS via BaTiO_3 is enhanced by 4.8 and 3.8 times, respectively. Since then, various piezo-activation materials of PMS systems, including MoS_2 , BaTiO_3 , $\text{BaTiO}_3/\text{MoS}_2$ heterojunction, and so on, have been developed to trigger piezoelectric polarization charges for PMS activation to remove organic contaminants in water

* Corresponding authors.

** Corresponding author at: Guangdong Key Laboratory of Environmental Pollution and Health, School of Environment, Jinan University, Guangzhou 511443, PR China.

E-mail addresses: zhaichunyang@nbn.edu.cn (C. Zhai), yangjl@jnu.edu.cn (J. Yang), zhumingshan@jnu.edu.cn (M. Zhu).

<https://doi.org/10.1016/j.apcatb.2023.122399>

Received 30 October 2022; Received in revised form 27 December 2022; Accepted 12 January 2023

Available online 14 January 2023

0926-3373/© 2023 Elsevier B.V. All rights reserved.

[21–27]. However, the poor efficiency of piezo-polarization-induced charge separation on the surface of piezoelectric materials and the low affinity of polarization electrons with PMS restrict PMS activation and ROS generation. To improve the PMS utilization efficiency, a piezocatalyst with rapid separation of local accumulated piezo-polarization charges and rich active sites on the surface needs to be developed.

Mesocrystals are highly ordered mesoporous superstructures with rich defects and high internal porosity, which can effectively facilitate anisotropic charge migration and manipulate the affinity toward reactants [28,29]. Specially, these abundant defects and orderly arranged nanocrystals provide rich active sites, affording mesocrystals as promising PMS piezo-activators for water treatments. In this work, we fabricated a twin-brush ZnO piezoelectric mesocrystal (TB-ZnO) with abundant oxygen vacancies to optimize piezo-polarization charge migration and provide rich active sites. Taking ibuprofen (IBP) as the representative organic pollutant, the effects of oxygen vacancies in TB-ZnO for the piezo-activation of PMS toward IBP removal were investigated. This fabricated TB-ZnO piezoelectric mesocrystal shows ultrahigh activity toward PMS activation. Its PMS utilization efficiency obviously exceeds the benchmarked PMS activators, including non-mesocrystal ZnO nanorods (NR-ZnO) and other commonly reported piezocatalysts. We elucidated the role of oxygen vacancies on the enrichment of the reactants and piezo-electron regulation, as well as the underlying mechanisms of piezo-activated PMS catalytic reactions using TB-ZnO via experiments (quenching experiments and spin-trapping techniques) and theoretical calculations (including COMSOL, density functional theory (DFT)). Moreover, the IBP degradation pathways and products toxicity were proposed based on the results of liquid chromatography time-of-flight-mass spectrometer (LC-TOF-MS) analysis and dual descriptor (DD) value calculations.

2. Experimental methods

2.1. Characterization of catalysts

The morphologies of as-prepared ZnO were observed using a scanning electron microscope (SEM, JEOL JSM-6330F) and transmission electron microscopy (TEM, JEOL JEM-2100F). X-ray diffraction (XRD, Bruker D2 Phaser) was determined to verify the crystal structure of as-prepared ZnO. The elemental composition and valance of as-prepared ZnO were examined by X-ray photoelectron spectroscopic (XPS, ESCA-LAB 250 photoelectron spectrometer, Thermo-VG Scientific). UV-visible diffuse reflectance spectra (UV-vis DRS, JASCO V-770) was used to determine the existence of oxygen vacancy. Piezoresponse force microscopy (PFM, Asylum Research Cypher) was carried out to verify the piezoelectric property of the as-prepared ZnO. ROS in the reaction solution and structural defects (i.e., atomic vacancies) of solid-state specimens were measured by an electron spin resonance spectroscopy (ESR, Bruker 5000) under experimental setting included temperature = 298.02 K, microwave frequency = 9.4 GHz, center field = 336 mT, and modulation = 0.1. High-performance liquid chromatography (HPLC, Shimadzu, LC-16) was equipped with a UV detector and a column of 2.1 mm × 100 mm (1.8 μm, Agilent SB-C18). Under the 223 nm detection wavelength, the mobile phase ratio was 75:25, composed of acetonitrile and 0.1% formic acid at a rate of 0.1 mL min⁻¹ for IBP measurement. The degradation products of IBP were detected by liquid chromatography time-of-flight-mass spectrometer (LC-TOF-MS, AB Sciex Triple TOF 5600). The mobile phase ratio was composed of acetonitrile and 0.1% formic acid with a volume ratio of 75: 25 and a mass range of 50–500 *m/z* at the positive ion mode.

2.2. Preparation of catalysts

Twin-brush hierarchical structures of ZnO mesocrystal (TB-ZnO): Typically, 0.7 g gum Arabic was dissolved into 210 mL deionized water, followed by adding 6.23 g Zn (NO₃)₂ and 2.94 g hexamethylene

tetramine (HMTA) under 50 °C with the stirring steadily. After mixing, the dispersion was transferred to a 250 mL bottle, which was sealed and maintained in a water bath at 80 °C for 21 h. Subsequently, the precipitate was washed with deionized water twice, dried at 60 °C, and then annealed at 300 °C for three h in a muffle furnace [30].

Nanorod ZnO non-mesocrystal (NR-ZnO): Briefly, Zn(NO₃)₂ (0.0105 M) was dissolved in 210 mL ethanol, and then added NaOH (2.1 M) under a steady stirring at 25 °C. Subsequently, 4.2 g hexadecyltrimethylammonium bromide (CTAB) and 105 mL ethylenediamine (EDA) were dissolved into the previous solution and stirred for five days. Hereafter, the as-prepared ZnO nanorod was washed with 99.9% ethanol and deionized water three times, then dried in an oven at 60 °C.

2.3. Experimental setup

Batch experiments were carried out in a glass beaker filled with 40 mL of IBP solution under magnetic stirring. Typically, 20 mg of catalysts (0.5 g L⁻¹) was dispersed in a 40 mL IBP (15 mg L⁻¹) solution. Then, 20 mg of PMS (0.5 g L⁻¹) was added. Before the reaction, each catalyst was dispersed in the IBP solution magnetically stirring in the dark for 30 min to evaluate the absorption performance. Afterward, the suspension was treated by ultrasonic vibration with a frequency of 40 kHz and a power of 100 W in the dark for 50 min. At certain time intervals, 0.5 mL solution was withdrawn and filtered through a 0.22 μm syringe filter. Then, 0.5 mL methanol was added to the filtrate, and the mixture was analyzed by HPLC immediately.

The utilization efficiency of PMS was determined by a UV-visible spectrometer, as reported previously [31]. In a typical procedure, a 0.5 mL liquid sample was added into a 10 mL mixed solution of KHCO₃ and KI (1.25 g KHCO₃ + 10 g KI dissolved in 250 mL deionized water). The subsequent solution was initially hand shaken and then analyzed by a UV-visible spectrometer at 352 nm. The PMS utilization efficiency during the catalytic reactions was calculated by correlating the PMS decomposition ratio with the IBP removal ratio, respectively, following Eq. (1), where [IBP] and [PMS] are the total decomposed amounts of IBP and PMS, respectively.

$$\text{PMS utilization efficiency} = \frac{\Delta[\text{IBP}]}{\Delta[\text{PMS}]} \quad (1)$$

The details, including chemicals, catalyst preparation, and theoretical computations, were presented in the [Supporting Information \(Text S1\)](#).

3. Results and discussion

3.1. Reactivity of the TB-ZnO for PMS activation

The structures of two types of as-prepared ZnO were investigated by XRD, SEM, and TEM. All characteristic diffraction peaks in these catalysts match well with the hexagonal structure of ZnO (JCPDS card no. 36-1451) (see Fig. S1). The SEM images in Fig. 1a and b show that TB-ZnO with a symmetric twin-brush-like structure consists of numerous ZnO nanorods aligned in parallel, revealing the orientated attachment of nanocrystallites in TB-ZnO. The selected area electron diffraction (SAED) patterns were collected from the top view of TB-ZnO in Fig. 1c. The single-crystal-like structure reveals its mesocrystal nature due to the oriented assembly of nanorods where the constituting crystallites are arranged along a shared crystallographic register. The clear discrete diffraction spots correspond to the wurtzite structure of ZnO. The lattice fringes (0.281 nm) observed in TB-ZnO correspond well to the (100) lattice planes (Fig. S2). The (101 $\bar{0}$) nonpolar surfaces are the main exposed facets in TB-ZnO [32]. For NR-ZnO, the TEM image demonstrates its nanorod-like structure (Fig. S3).

Next, the piezocatalytic performances of two as-prepared ZnO toward IBP degradation were explored. IBP, as a nonsteroidal anti-inflammatory drug frequently occurring in surface water, was selected

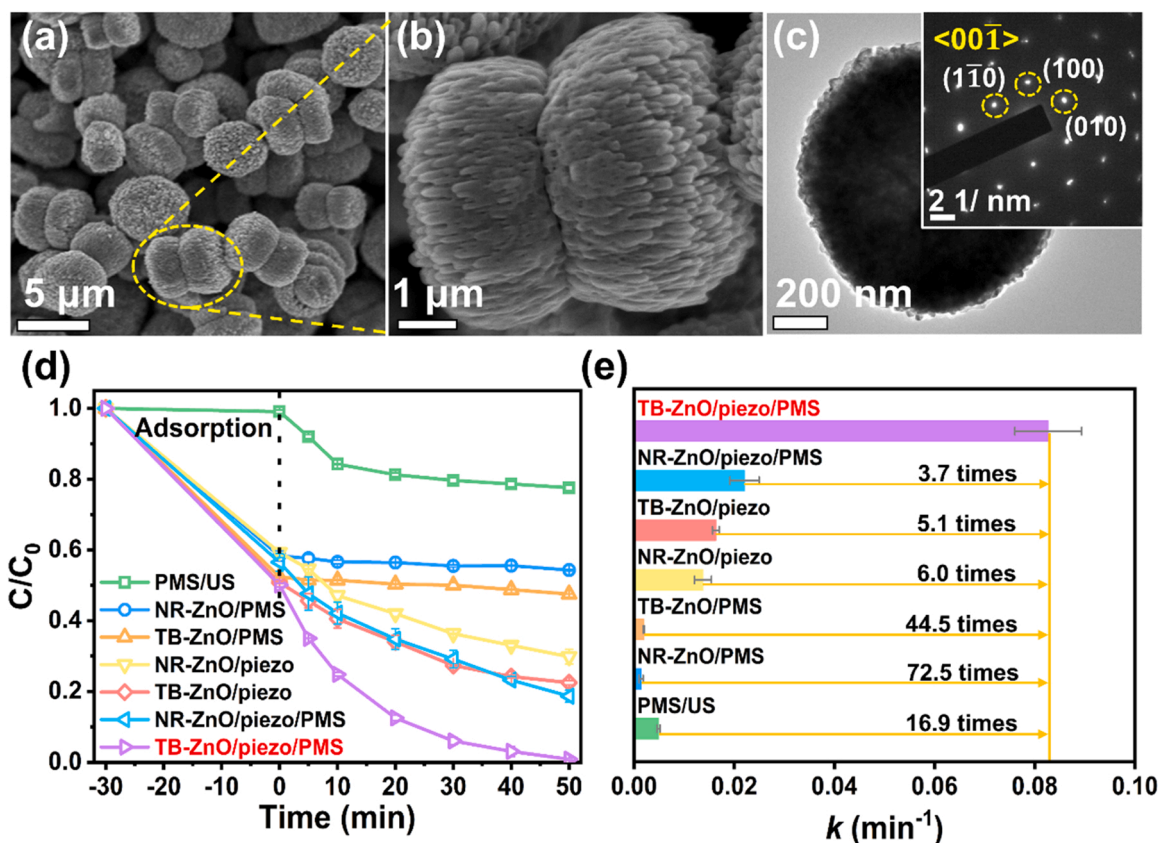


Fig. 1. (a, b) SEM and (c) TEM (top view) images of TB-ZnO, the inset in Fig. 1c is the SAED pattern of TB-ZnO. (d) Degradation efficiencies and (e) kinetic fittings of IBP degradation in different catalytic systems.

as the target pollutant resistant to the conventional water treatment processes [33]. First, 41.7% and 47.7% of IBP removal were achieved via 30 min adsorption by using NR-ZnO and TB-ZnO without ultrasound (US) and PMS, respectively (see Fig. S4), revealing the high affinity of as-prepared ZnO toward IBP. Meanwhile, the IBP removal efficiencies of NR-ZnO/PMS (45.7%) and TB-ZnO/PMS (52.4%) were only slightly higher than that of bare ZnO systems, indicating that ZnO could not activate PMS via heterogeneous catalysis (see Fig. 1d). Afterward, ultrasound was used to trigger the generation of piezoelectricity in ZnO. In the PMS/US process without catalyst, only 22.8% degradation efficiency was obtained in 50 min. Meanwhile, TB-ZnO removed 80.0% of IBP in 50 min under the US without PMS, which is significantly higher than the bare TB-ZnO system, confirming that the US can motivate TB-ZnO to

produce piezo-charges to trigger the redox reaction. Notably, when ZnO/piezo systems were combined with PMS, significant improvement in IBP removal was observed for TB-ZnO (~100% IBP removal) relative to NR-ZnO (84.2%), revealing the great activity of TB-ZnO toward piezocatalytic PMS activation. Fig. 1e shows a comparison of the IBP degradation kinetics in those systems. The rate constant k of TB-ZnO/piezo/PMS process (0.083 min^{-1}) is 3.7 times higher than NR-ZnO/piezo/PMS process (0.022 min^{-1}), 5.1 times higher than TB-ZnO/piezo process, and 44.5 times higher than TB-ZnO/PMS process (without ultrasound), revealing piezoelectric PMS activation process by TB-ZnO is highly efficient towards antibiotic removal.

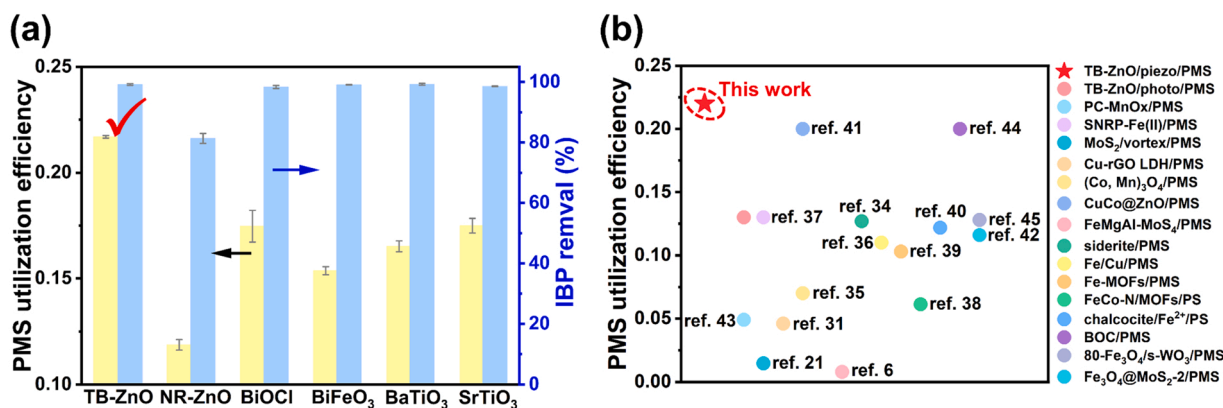


Fig. 2. (a) PMS utilization and IBP degradation efficiencies under different catalysts/piezo/PMS systems. (b) Comparison of PMS utilization efficiencies of this work with other reported PMS activation systems.

3.2. The utilization efficiency of PMS

The corresponding utilization efficiency of PMS in the TB-ZnO/piezo/PMS process was detected by the titration method. As shown in Fig. 2a, the TB-ZnO mesocrystal offered the highest PMS utilization efficiency (0.22) compared to NR-ZnO non-mesocrystal (0.12) and other common piezocatalysts such as BiOCl (0.17), BiFeO₃ (0.15), BaTiO₃ (0.16), and SrTiO₃ (0.17). ZnO has been widely reported as a photocatalyst for application in environmental remediation, and thus, the PMS utilization efficiency of the TB-ZnO/photo/PMS process was also compared. Notably, the PMS utilization efficiency of the TB-ZnO/piezo/PMS process was 1.69 times higher than that of the TB-ZnO/photo/PMS process (0.13), suggesting that the piezocatalytic PMS activation process via TB-ZnO is more favorable for PMS activation through photocatalytic activation. Besides, the PMS utilization efficiency in TB-ZnO/piezo/PMS process was also higher than the other widely reported homogeneous and heterogeneous PMS systems (Fig. 2b) [6,21,31,34–45], revealing the current TB-ZnO/piezo/PMS process was extremely reactive towards PMS activation. The above results indicate that the environmental micro-energy driven piezocatalysis via mesocrystal appears to be a promising and high-efficiency strategy to intensify AOPs oxidation.

3.3. Piezoelectric ability of TB-ZnO

A higher piezoelectric potential can accelerate the generation of ROS, which may significantly improve the piezo-catalytic activity. The piezoelectric property and potential were investigated to explore the underlying mechanism responsible for IBP degradation and PMS activation in TB-ZnO/piezo/PMS process. First, the distribution of piezoelectric potential in the TB-ZnO was simulated by constructing the rod-like ZnO with (101 $\bar{0}$) nonpolar surfaces as a model via a computational

simulation using COMSOL multiphysics software package (Fig. 3a–c). The piezoelectric potential in the TB-ZnO is distributed mainly at the bottom of the rod. The surface piezoelectric potential increases as the applied force increase from 10 to 100 N m⁻², indicating that the mechanical deformation induces the piezoelectric effect in TB-ZnO to accelerate the separation of charges.

The piezo-charges generation and transportation in that as-prepared ZnO were investigated by piezoresponse force microscopy (PFM) and transient piezoelectric current responses. The PFM hysteresis loop (green square) and amplitude butterfly loop (blue circle) of the as-prepared ZnO are shown in Fig. 3d and e. A local hysteresis loop where the phase angle exhibited a $\sim 180^\circ$ change under the reversal of a 10 V direct current DC bias field could be observed in TB-ZnO, suggesting a complete polarization switching process. This phenomenon indicated that a significant piezo-potential was generated when the atomic force microscope tip was scanning across the surface of the TB-ZnO. The maximum amplitude of butterfly loops of TB-ZnO is about 400 pm, while NR-ZnO exhibited a negligible piezoelectric response (0.6 pm). The current response under the piezoelectric field of catalysts was measured to investigate the polarization field-induced charge transportation behaviors (Fig. 3f). TB-ZnO exhibited a prompt and reproducible current response to the on/off sonication, stemming from the piezo-electrons. The piezoelectric current intensity of TB-ZnO is 7.8 times higher than that of NR-ZnO, demonstrating the enhanced formation and separation of piezo-charges in TB-ZnO. Therefore, TB-ZnO might exhibit a stronger piezoelectric activity. These results confirmed the stronger piezoelectric response in TB-ZnO mesocrystals than that of commonly non-mesocrystal of NR-ZnO.

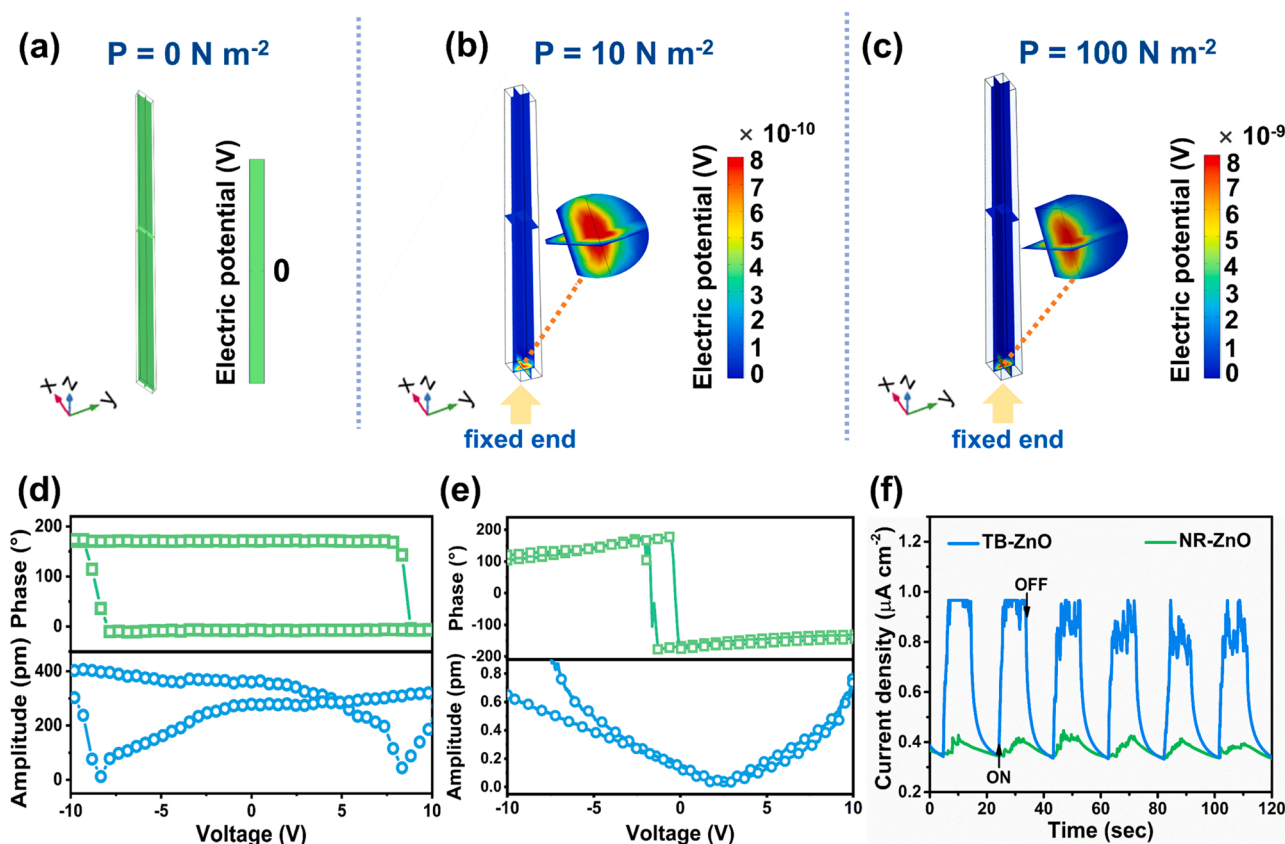


Fig. 3. COMSOL simulation for the piezoelectric potential distribution of TB-ZnO with a force of (a) 0, (b) 10, and (c) 100 N m⁻² applied along the z-axis, respectively. PFM phase hysteresis loop (green square) and amplitude butterfly loop (blue circle) of (d) TB-ZnO and (e) NR-ZnO. (f) Transient piezoelectric current responses of as-prepared TB-ZnO and NR-ZnO with (on) and without (off) ultrasonic vibration.

3.4. Oxygen vacancies effects on PMS piezo-activation

Given the considerable difference in piezoelectric property of the as-prepared ZnO, the surface composition and valence state of two as-prepared ZnO were investigated by XPS. The binding energies of 1021 and 1044 eV correspond to Zn 2p_{3/2} and Zn 2p_{1/2}, respectively (Fig. S5). The peaks of O 1s at the binding energies of 530, 531, and 533 eV are assigned to lattice oxygen (O_{lattice}), surface-adsorbed oxygen species (O_{ads}), and the hydroxyl/carbonate species (O_{surf}), respectively (Fig. 4a) [46,47]. TB-ZnO with an O_{lattice} proportion of 67.1% was lower than that of NR-ZnO (75.5%), whereas the proportions of O_{ads} + O_{surf} were higher, attributed to the oxygen vacancies that result in greater adsorption of surface oxygen species. The atomic vacancies in those specimens were further detected by ESR (Fig. 4b). The ESR results showed that TB-ZnO mesocrystal possesses more oxygen defects than NR-ZnO, due to the mesocrystals nature [32]. Moreover, UV-vis diffuse reflectance spectra (UV-vis DRS) were used to investigate the presence of oxygen vacancy, and the discussion and result are shown in Text S2 and Fig. S6. These results suggest abundant oxygen vacancies exist in TB-ZnO.

To get a deep understanding of the role of oxygen vacancies on the activity of piezo-catalytic PMS activation, we carried out theoretical calculations and reactive species analysis. The existence of oxygen vacancies can promote the adsorption and activation of oxygen-containing molecules, further providing more oxygen-containing active species for redox reactions. The adsorption behavior of TB-ZnO was simulated by DFT calculations. The adsorption energy (E_{ads}) of reactants in oxygen vacancies rich ZnO and defect-free ZnO was calculated, and the outcomes were displayed in Fig. 5a and Table S1. The reactants O₂, H₂O, PMS, and IBP are both oxygen-containing molecules. Oxygen vacancy-rich ZnO exhibited remarkably lower E_{ads} toward the target molecules (O₂, H₂O, PMS, and IBP) compared with defect-free ZnO, and the adsorption of PMS and H₂O were more favorable. Thus, oxygen vacancies could act as adsorption centers to capture oxygen-containing molecules and facilitate redox reactions. Besides, the higher affinity toward PMS could enhance the PMS activation, thus improving the efficiency of PMS utilization. Given that the d-band center model is known to be a good descriptor of the chemical reactivity of transition metal catalysts, the d-band center of oxygen vacancies rich ZnO and defect-free ZnO were simulated. As shown in Fig. 5b, the d-band centers of defect-free ZnO and oxygen vacancies rich ZnO were calculated to be -2.555 and -1.634 eV, respectively. The upshift of the d-band center in vacancy-rich ZnO can increase the adsorption of oxygen-containing reactants and strengthen the interaction between the adsorbate and

catalyst surface [48,49].

The corresponding calculated density of state in Fig. 5c further verified that the vacancy-rich ZnO owns an increased density of state compared with that of defect-free ZnO. Meanwhile, the oxygen vacancies resulted in several new defect levels [50]. These new defect levels could act as exciton trapping centers to efficiently promote piezo-electrons transfer to the conduction band, facilitate the separation of carriers, and enable more electrons to participate in the redox processes [51–53]. Moreover, the charge density difference was further simulated to monitor the electronic structure of ZnO samples after contact with PMS. As shown in Fig. 5d, there was overt charge accumulation around Zn and charge depletion around O in vacancy-rich ZnO, and the length of O-O bond in PMS was remarkably prolonged (1.47047 Å) compared with vacancy-free ZnO (1.4678 Å), demonstrating that the existence of oxygen vacancies could facilitate the breakage of O-O bond in PMS, thus producing more ROS to enhance the piezocatalytic activity. Therefore, the oxygen vacancies in TB-ZnO served as active sites that not only facilitate the reactants capture, but also increase the electron density and the piezo-charge mobility, thus providing more electrons to participate in catalytic reactions.

3.5. Application feasibility of TB-ZnO/piezo/PMS system in water treatment

To assess the applicability feasibility of the TB-ZnO/piezo/PMS system, the effect of the different anions, the treatment for real water matrices, the recycling ability of catalyst, the possible degradation products, and their toxicity evaluation were systematically assessed on IBP removal. The effect of reaction conditions, including TB-ZnO dosage, PMS concentration, and initial IBP concentration on catalytic IBP removal in the TB-ZnO/piezo/PMS process was investigated. The detailed discussion was presented in the Supporting information (see Text S3, Fig. S7–9). The optimal reaction condition could be achieved at a TB-ZnO dosage of 0.5 g L⁻¹, a PMS concentration of 0.5 g L⁻¹, and initial pH of 7.

As shown in Fig. 6a, TB-ZnO exhibited an excellent degradation efficiency for IBP in a wide pH range from 3 to 11. Even under very alkaline conditions, IBP was almost completely degraded within 50 min. In general, the activity of metal catalysts is susceptible to changes in pH. Because the surface hydroxyl groups tend to form at the surface metal sites in an aqueous solution. However, TB-ZnO successfully avoided the pH effect on the activity because metal species may be less participate in activating PMS, but mainly relied on the single electrons of the oxygen vacancies [54]. In the previous literature, the oxygen vacancies

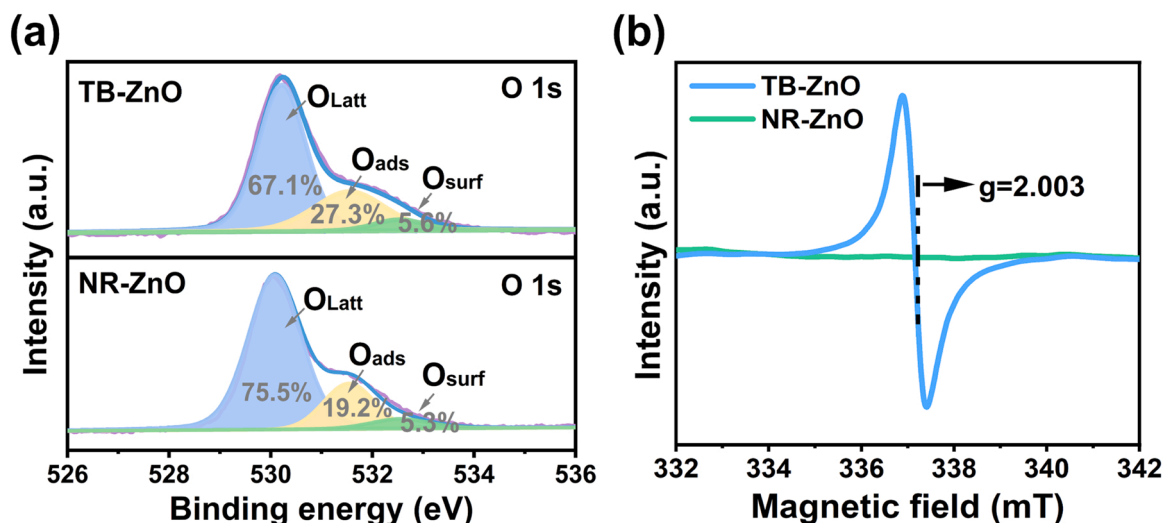


Fig. 4. (a) XPS spectra of O 1s, and (b) ESR spectra of TB-ZnO and NR-ZnO.

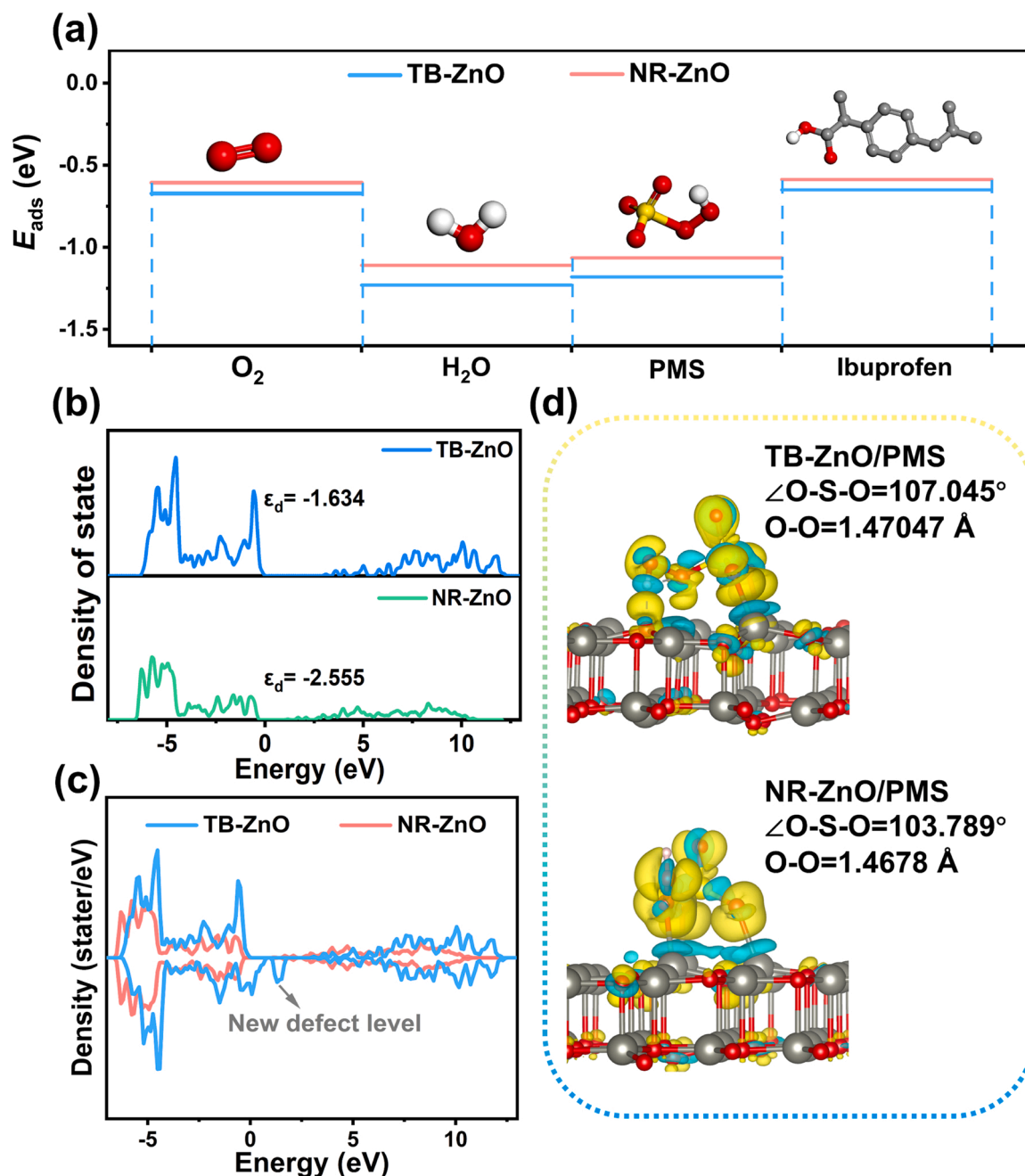


Fig. 5. (a) The adsorption energy of target molecules, (b) D-band center, (c) electrostatic potential images, and (d) the charge density difference at the interface between ZnO samples and PMS.

dominated the activation of the H_2O_2 system with the same result, which might be attributed to the oxygen vacancies in the catalytic process that could mitigate the negative effect of the pH [55]. This pH independence, also observed in other PMS-based oxidation processes, was one significant advantage in this system compared with multiple oxidation catalysts, whose efficiency was significantly affected by the pH. TB-ZnO/piezo/PMS process shows good application potential for efficiently degrading pollutants on a broader pH working window.

Furthermore, the impacts of inorganic ions (HCO_3^- , PO_4^{3-} , NO_3^- , and Cl^-) and natural organic matter on IBP degradation were investigated. As Fig. 6b illustrates, the addition of PO_4^{3-} , NO_3^- , and Cl^- showed negligible inhibition on the performance of the TB-ZnO/piezo/PMS process, in which the degradation efficiencies of IBP were 99.2%, 91.5%, and 93.9% within 50 min, respectively. However, the degradation efficiencies of IBP slightly decreased to 82.4% in the presence of

HCO_3^- because HCO_3^- could react with $\text{SO}_4^{\bullet-}$ to generate less reactive carbonate radicals [56].

Afterward, four types of water matrices, including tap water (laboratory), rain water (Guangzhou), river water (Shanghai), and medical wastewater (Qingyuan) were chosen to replace deionized water to evaluate the IBP degradation performance in real water matrices (Fig. 6c). The detailed parameters of real water matrices were shown in Table S2. IBP degradation efficiencies reached up to 85.4%, 83.7%, 81.8%, and 75.4% in tap water, rainwater, river water, and medical wastewater, respectively, indicating the excellent availability of TB-ZnO/piezo/PMS process in treating IBP in natural water. The slightly decreased degradation efficiency of IBP in natural water compared with deionized water was ascribed to the complex water environment (pH, inorganic ions, fungus, etc.) that substantially consumed reactive species. The consistent performance over a wide pH and negligible

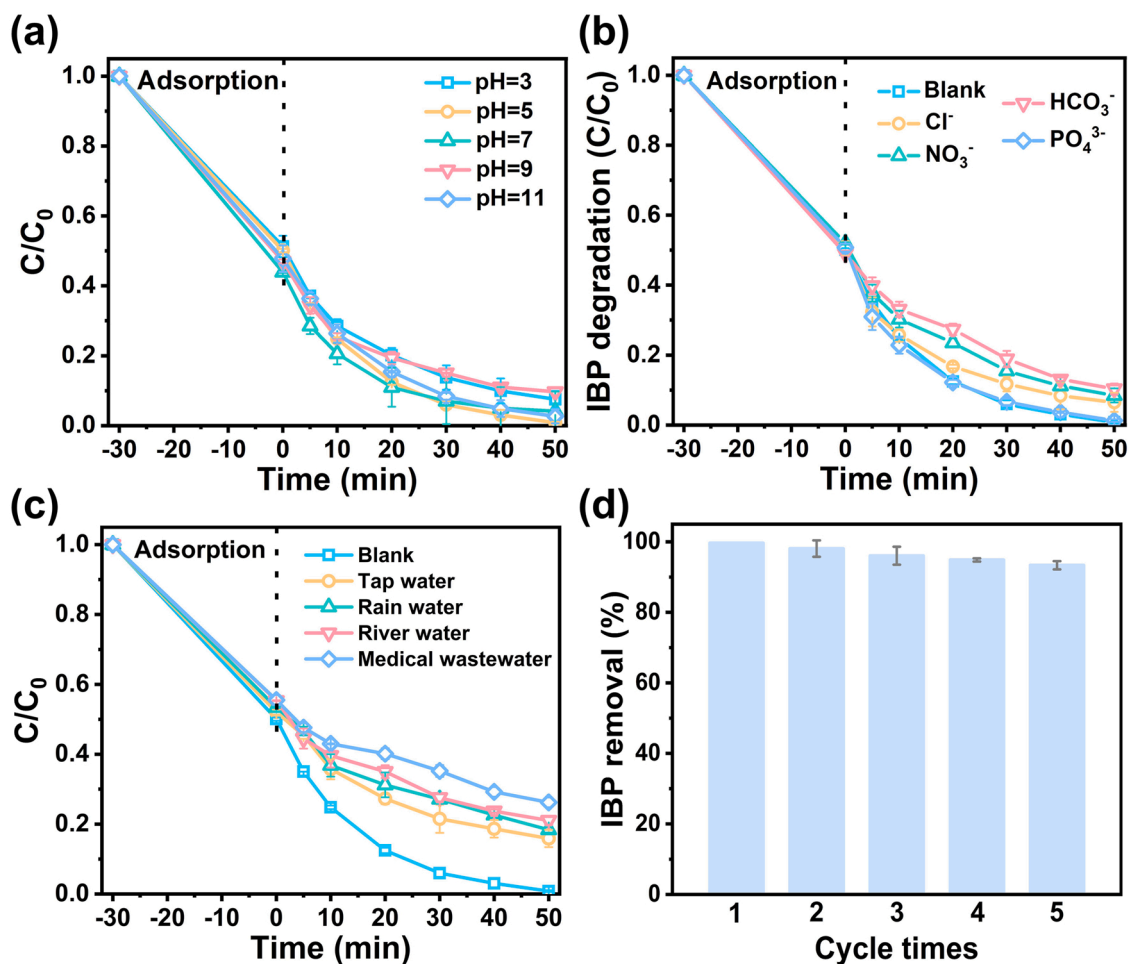


Fig. 6. Influences of (a) pH, (b) co-existing anions, (c) real water matrices, and (d) re-cycle experiments in the TB-ZnO/piezo/PMS process for IBP degradation.

influence of anions or a complex water environment suggested that the TB-ZnO/piezo/PMS system was promising for natural wastewater treatment. The catalytic stability was evaluated via cycle experiments and structure characterization of used TB-ZnO. The degradation efficiencies of IBP in the TB-ZnO/piezo/PMS process were maintained at 82% after five cycles (Fig. 6d). Besides, the XRD pattern of TB-ZnO after five cycles showed no significant changes, confirming the excellent stability (Fig. S10). Moreover, the change of surface valence state of TB-ZnO before and after reaction was evaluated by XPS, and the results were discussed and shown in Text S4 and Fig. S11.

The possible degradation intermediates and reaction pathways of IBP in the TB-ZnO/piezo/PMS process were investigated through DFT calculation and LC-TOF-MS analysis. Based on the mass-to-charge ratio data (Fig. S12), 12 main by-products and the corresponding structure are identified, which were recorded as P1-P12 (Table S3). According to the results of the f_A^2 calculation, 1 C and 5 C with lower values were easily attacked by electrophilic oxidation species ($^1\text{O}_2$, $\text{O}_2^{\bullet-}$, HO^\bullet , and $\text{SO}_4^{\bullet-}$), and 6 C, 14 C, and 15 C with higher values were easily attacked by nucleophilic oxidation species (HO^\bullet and $\text{SO}_4^{\bullet-}$) (Fig. 7a, Table S4). According to the element ratios of H/C and O/C, all the intermediates of IBP were distributed in the Van Krevelen diagram which was divided into four quadrants with IBP as the coordinate origin (Fig. 7b and c) [57]. The intermediates were mainly located in quadrants I and III. Based on the ascertained intermediates, three possible pathways of IBP degradation were tentatively proposed (see Fig. 7d and Text S5). The IBP degradation undergoes hydroxylation, double bond destruction, and decarboxylation that ultimately convert IBP into smaller molecules with a TOC removal rate of 53.2% was realized (Fig. S13).

In addition, the toxicity of IBP and its degradation products were evaluated by the Toxicity Estimation Software Tool (T.E.S.T), which adopted the endpoint of acute toxicity (oral rat LC_{50} and LD_{50} as representatives) and presented in Table S5. Almost all degradation intermediates exhibited higher LD_{50} and LD_{50} values than IBP, illustrating that the acute toxicity was significantly reduced after reaction by TB-ZnO/piezo/PMS system (Fig. S14 and S15).

3.6. Proposed mechanism of PMS piezo-activation over TB-ZnO

Quenching experiments and ESR were performed to identify the reactive species and their quantitative contributions to the IBP degradation in the TB-ZnO/piezo/PMS process. The generation of reactive species provides a prerequisite for IBP oxidation. Quenching experiments were carried out using methanol (MeOH) as the radical trapping for $\text{SO}_4^{\bullet-}$ and HO^\bullet , while tert-butanol (TBA), ascorbic acid (AA), L-histidine (L-his), silver nitrate (AgNO_3) and potassium iodide (KI) as the scavengers for HO^\bullet , $\text{O}_2^{\bullet-}$, $^1\text{O}_2$, electrons and holes respectively. As shown in Fig. S16, the IBP degradation efficiencies dramatically decreased from ~100% to 50.4% and 53.7%, in the presence of TBA and MeOH, respectively, indicating HO^\bullet might play a significant role in the TB-ZnO/piezo/PMS system. The addition of AA and L-his inhibited the IBP degradation by 29.0% and 19.9%, suggesting that $\text{O}_2^{\bullet-}$ and $^1\text{O}_2$ also participated in the IBP degradation. The ESR results were shown in Fig. S17, no obvious signal could be observed in both PMS alone and ultrasound alone systems, suggesting that there was either negligible generation of ROS in these systems. Meanwhile, the signal of DMPO- HO^\bullet , DMPO- $\text{SO}_4^{\bullet-}$, DMPO- $\text{O}_2^{\bullet-}$ and TEMP- $^1\text{O}_2$ were detected in the TB-

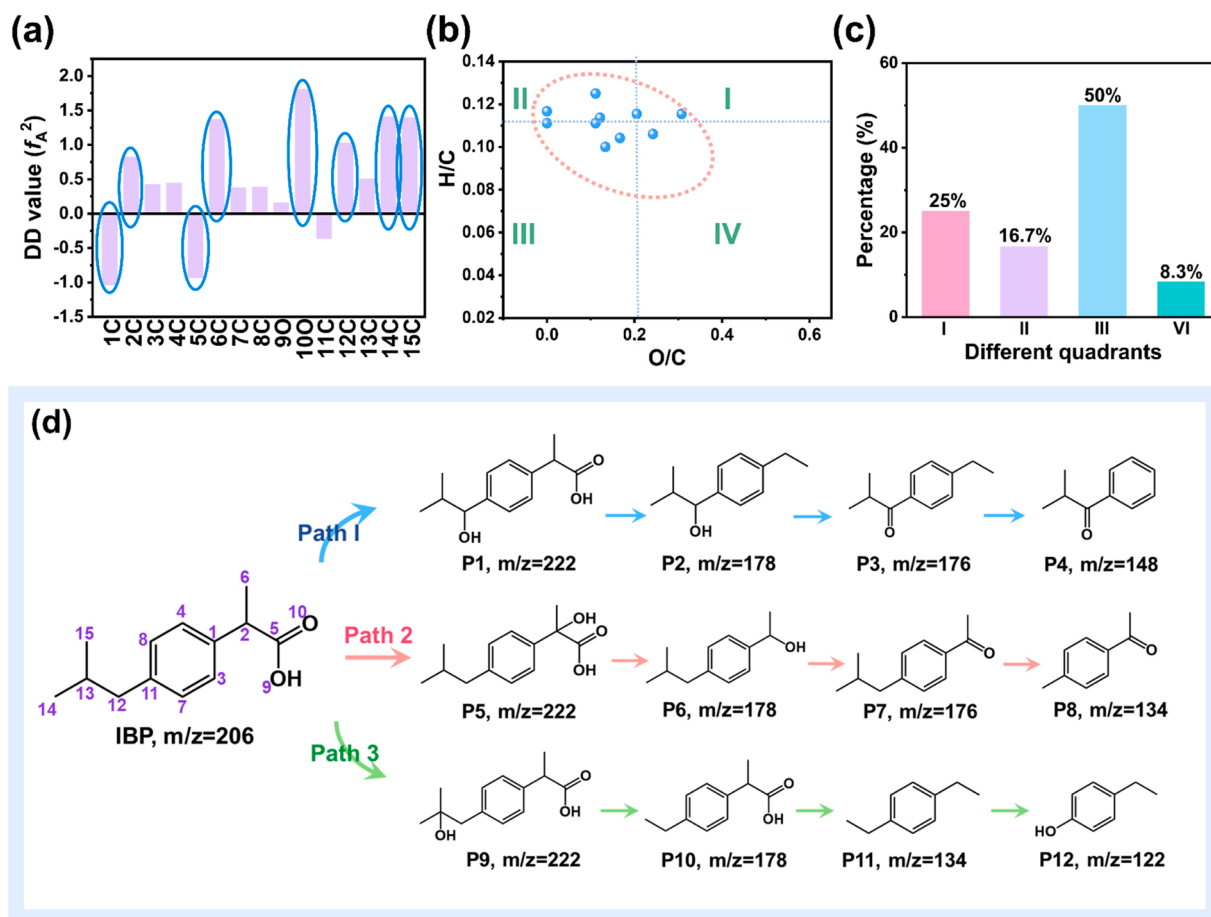


Fig. 7. (a) DFT calculations of IBP at B3LYP/6-31+G(d,p) level. (b) (c) Van Krevelen diagrams of degradation products, and (d) degradation pathways of IBP degradation.

ZnO/piezo/PMS process (Fig. S18), which was consistent with the results of quenching experiments, indicating that HO^\bullet played a dominant role in the IBP removal, while $\text{SO}_4^{\bullet-}$, $\text{O}_2^{\bullet-}$, and $^1\text{O}_2$ were also involved in the reaction. The higher contribution of HO^\bullet could be attributed to the high affinity of H_2O and PMS on TB-ZnO, which facilitates the formation of HO^\bullet ($\text{SO}_4^{\bullet-} + \text{H}_2\text{O} \rightarrow \text{HO}^\bullet + \text{H}^+ + \text{SO}_4^{2-}$).

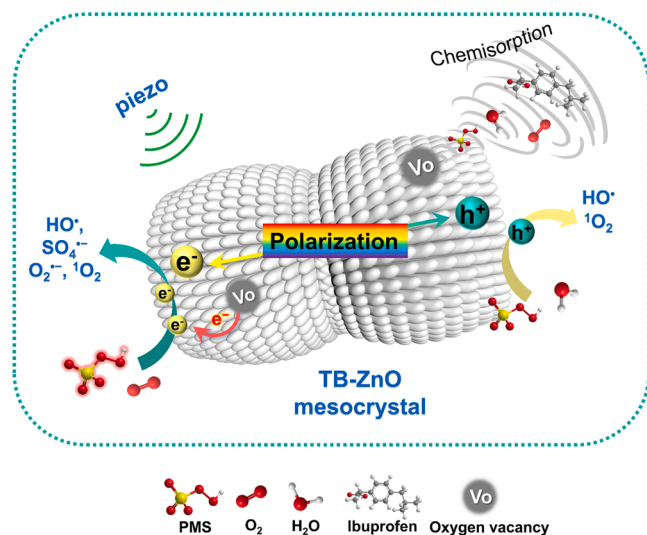
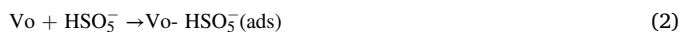


Fig. 8. Proposed IBP degradation mechanism in the TB-ZnO/piezo/PMS process.

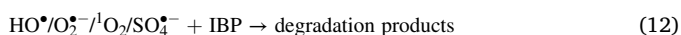
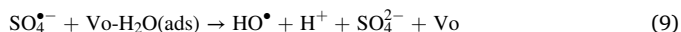
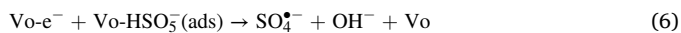
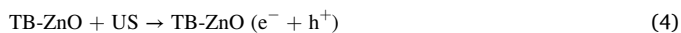
Above all, the reaction mechanism for IBP degradation using TB-ZnO/piezo/PMS process is proposed in Fig. 8. In principle, the introduction of oxygen vacancies enabled ZnO to change internal structure for a stronger non-overlapping of positive and negative ion centers, which contributed to building the electric-field with greater polarization intensity. More polarized charges in the electric-field could bring about more free carriers to boost catalytic redox reactions. Under ultrasound, the PMS and H_2O molecules were chemisorbed onto the oxygen vacancies of TB-ZnO (Eqs. 2 and 3). Meanwhile, the IBP and O_2 molecules also accumulate around the oxygen vacancies of TB-ZnO mesocrystal. Under stress derived from ultrasound, polarized positive and negative charges were produced on the opposite surfaces of TB-ZnO mesocrystal and subsequently established an internal polarization electric field (Eq. 4). Simultaneously, the presence of oxygen vacancies adjusted the intrinsic charge carrier density and electron migration due to the formation of new defect levels, resulting in an electron-rich center at Zn-oxygen vacancies of TB-ZnO mesocrystal (Eq. 5).

Then, the chemisorbed PMS and O_2 can obtain electrons from the electron-rich center to generate ROS ($\text{SO}_4^{\bullet-}$, HO^\bullet , $\text{O}_2^{\bullet-}$, and $^1\text{O}_2$) while HO^\bullet is the main reactive species (Eqs. 6–11) to achieve efficient decomposition of IBP (Eq. 12). Moreover, the consumed electrons could be continuously replenished via piezoelectric process to maintain the efficient and sustainable degradation of IBP. Based on the results above, the most catalytically active sites should be at the oxygen vacancies of TB-ZnO because the presence of oxygen vacancies can promote the specific adsorption of reactants (PMS, H_2O) and enable more electrons to participate in the reactions, thereafter, promoting PMS utilization and H_2O activation for improved IBP degradation.

(1) Chemisorption:



(2) Piezo-activation:



4. Conclusions

This work constructed TB-ZnO via defect engineering for boosting the piezo-activation of PMS. The system showed state-of-the-art PMS utilization efficiency, rapid reaction kinetics, robust stability, and availability toward complete IBP degradation in water. First, considering the low PMS cost, high IBP degradation efficiency, and environmental benignity of ZnO, the piezo-activation of PMS via TB-ZnO mesocrystal can be applied to large-scale wastewater treatment facilities based on PMS-AOPs technologies. Moreover, the synthetic process of TB-ZnO is facile and cost-effective, which is beneficial to the large-scale production of the catalyst. Furthermore, this study unravels the high-activity origin of the TB-ZnO mesocrystal from the presence of oxygen vacancies which not only promote the surface enrichment of reactants but also adjust the electronic structure. These features provide more electrons to participate in PMS activation, which can offer valuable guidance for the design of efficient PMS activation system toward sustainable environmental remediation.

CRediT authorship contribution statement

Minxian Zhang: Methodology, Data curation, Formal analysis, Writing - original draft. **Hengcong Tao:** Methodology, Data curation, Formal analysis. **Chunyang Zhai:** Investigation, Methodology, Writing - review & editing. **Jingling Yang:** Supervision, Methodology, Writing - review & editing, Funding acquisition. **Yingtang Zhou:** Methodology, Formal analysis. **Dehua Xia:** Formal analysis. **Gabriele Comodi:** Investigation. **Mingshan Zhu:** Conceptualization, Supervision, Writing - review & editing, Funding acquisition.

Declaration of Competing Interest

The authors declare that they have no known competing financial interests or personal relationships that could have appeared to influence the work reported in this paper.

Data availability

Data will be made available on request.

Acknowledgements

The study was financially supported by the National Natural Science Foundation of China (No. 22006051), the Science and Technology Program of Guangzhou (Nos. 202201020545, 202102020325), Guangdong Basic Applied Basic Research Foundation (Nos. 2020B1515020038, 2022A1515010655), the Pearl River Talent Recruitment Program of Guangdong Province (No. 2019QN011148), and the Research Fund Program of Guangdong Provincial Key Laboratory of Environmental Pollution Control and Remediation Technology (2020B1212060022). M. Zhang appreciates to Special Funds for the Cultivation of Guangdong College Students' Scientific and Technological Innovation ("Climbing Program" Special Funds, No. pdjh2022a0054).

Appendix A. Supporting information

Supplementary data associated with this article can be found in the online version at doi:10.1016/j.apcatb.2023.122399.

References

- [1] J. Lee, U. Von Gunten, J.-H. Kim, Persulfate-based advanced oxidation: critical assessment of opportunities and roadblocks, *Environ. Sci. Technol.* 54 (2020) 3064–3081.
- [2] J. Yang, M. Zhu, D.D. Dionysiou, What is the role of light in persulfate-based advanced oxidation for water treatment? *Water Res.* 189 (2021), 116627.
- [3] W. Ren, C. Cheng, P. Shao, X. Luo, H. Zhang, S. Wang, X. Duan, Origins of electron-transfer regime in persulfate-based nonradical oxidation processes, *Environ. Sci. Technol.* 56 (2022) 78–97.
- [4] S. He, Y. Chen, X. Li, L. Zeng, M. Zhu, Heterogeneous photocatalytic activation of persulfate for the removal of organic contaminants in water: a critical review, *ACS EST Eng.* 2 (2022) 527–546.
- [5] P. Zhang, Y. Yang, X. Duan, Y. Liu, S. Wang, Density functional theory calculations for insight into the heterocatalyst reactivity and mechanism in persulfate-based advanced oxidation reactions, *ACS Catal.* 11 (2021) 11129–11159.
- [6] J. Ali, L. Wenli, A. Shahzad, J. Iftikhar, G.G. Aregay, I.I. Shahib, Z. Elkhilfi, Z. Chen, Z. Chen, Regulating the redox centers of Fe through the enrichment of Mo moiety for persulfate activation: a new strategy to achieve maximum persulfate utilization efficiency, *Water Res.* 181 (2020), 115862.
- [7] Y. Bao, W.-D. Oh, T.-T. Lim, R. Wang, R.D. Webster, X. Hu, Elucidation of stoichiometric efficiency, radical generation and transformation pathway during catalytic oxidation of sulfamethoxazole via peroxymonosulfate activation, *Water Res.* 151 (2019) 64–74.
- [8] S. Yang, S. Xu, J. Tong, D. Ding, G. Wang, R. Chen, P. Jin, X.C. Wang, Overlooked role of nitrogen dopant in carbon catalysts for peroxymonosulfate activation: Intrinsic defects or extrinsic defects? *Appl. Catal. B: Environ.* 295 (2021), 120291.
- [9] X. Li, S. Huang, H. Xu, Y. Deng, Z. Wang, Z.-Q. Liu, Molybdenum phosphide (MoP) with dual active sites for the degradation of diclofenac in Fenton-like system, *Chin. Chem. Lett.* 33 (2022) 1321–1324.
- [10] Q. Shi, S. Pu, X. Yang, P. Wang, B. Tang, B. Lai, Enhanced heterogeneous activation of peroxymonosulfate by boosting internal electron transfer in a bimetallic Fe₃O₄-MnO₂ nanocomposite, *Chin. Chem. Lett.* 33 (2022) 2129–2133.
- [11] R. Zhang, M. Chen, Z. Xiong, Y. Guo, B. Lai, Highly efficient degradation of emerging contaminants by magnetic CuO/Fe_xO_y derived from natural mackinawite (FeS) in the presence of peroxymonosulfate, *Chin. Chem. Lett.* 33 (2022) 948–952.
- [12] Y. Wang, Y. Xu, S. Dong, P. Wang, W. Chen, Z. Lu, D. Ye, B. Pan, D. Wu, C. D. Vecitis, Ultrasonic activation of inert poly (tetrafluoroethylene) enables piezocatalytic generation of reactive oxygen species, *Nat. Commun.* 12 (2021) 2200188.
- [13] X. Liu, L. Shen, W. Xu, W. Kang, D. Yang, J. Li, S. Ge, H. Liu, Low frequency hydromechanics-driven generation of superoxide radicals via optimized piezotronic effect for water disinfection, *Nano Energy* 88 (2021), 106290.
- [14] C. Jin, D. Liu, J. Hu, Y. Wang, Q. Zhang, L. Lv, F. Zhuge, The role of microstructure in piezocatalytic degradation of organic dye pollutants in wastewater, *Nano Energy* 59 (2019) 372–379.
- [15] J.-T. Lee, M.-C. Lin, J.M. Wu, High-efficiency cycling piezo-degradation of organic pollutants over three liters using MoS₂/carbon fiber piezocatalytic filter, *Nano Energy* 98 (2022), 107280.
- [16] C. Hu, J. Hu, Z. Zhu, Y. Lu, S. Chu, T. Ma, Y. Zhang, H. Huang, Orthogonal charge transfer by precise positioning of silver single atoms and clusters on carbon nitride for efficient piezocatalytic pure water splitting, *Angew. Chem. Int. Ed.* 61 (2022), e202212397.
- [17] C. Hu, F. Chen, Y. Wang, N. Tian, T. Ma, Y. Zhang, H. Huang, Exceptional cocatalyst-free photo-enhanced piezocatalytic hydrogen evolution of carbon nitride nanosheets from strong in-plane polarization, *Adv. Mater.* 33 (2021) 2101751.

- [18] W. Liu, P. Wang, Y. Ao, J. Chen, X. Gao, B. Jia, T. Ma, Directing charge transfer in chemical-bonded BaTiO₃@ReS₂ Schottky heterojunction for piezoelectric enhanced photocatalysis, *Adv. Mater.* 34 (2022) 2202508.
- [19] Y. Wen, J. Chen, X. Gao, H. Che, P. Wang, B. Liu, Y. Ao, Piezo-enhanced photocatalytic performance of ZnO nanorod array for pollutants degradation in dynamic water: Insight into the effect of velocity and inner flow field, *Nano Energy* 101 (2022), 107614.
- [20] S. Lan, Y. Chen, L. Zeng, H. Ji, W. Liu, M. Zhu, Piezo-activation of peroxymonosulfate for benzothiazole removal in water, *J. Hazard. Mater.* 393 (2020), 122448.
- [21] C. Yu, J. He, S. Lan, W. Guo, M. Zhu, Enhanced utilization efficiency of peroxymonosulfate via water vortex-driven piezo-activation for removing organic contaminants from water, *Environ. Sci. Ecotechnol.* 10 (2022), 100165.
- [22] Y. Chen, S. Lan, M. Zhu, Construction of piezoelectric BaTiO₃/MoS₂ heterojunction for boosting piezo-activation of peroxymonosulfate, *Chin. Chem. Lett.* 32 (2021) 2052–2056.
- [23] S. Liu, B. Jing, C. Nie, Z. Ao, X. Duan, B. Lai, Y. Shao, S. Wang, T. An, Piezoelectric activation of peroxymonosulfate by MoS₂ nanoflowers for the enhanced degradation of aqueous organic pollutants, *Environ. Sci. Nano* 8 (2021) 784–794.
- [24] D. Xia, Z. Tang, Y. Wang, R. Yin, H. He, X. Xie, J. Sun, C. He, P.K. Wong, G. Zhang, Piezo-catalytic persulfate activation system for water advanced disinfection: Process efficiency and inactivation mechanisms, *Chem. Eng. J.* 400 (2020), 125894.
- [25] F. Peng, R. Yin, Y. Liao, X. Xie, J. Sun, D. Xia, C. He, Kinetics and mechanisms of enhanced degradation of ibuprofen by piezo-catalytic activation of persulfate, *Chem. Eng. J.* 392 (2020), 123818.
- [26] S. Lan, B. Jing, C. Yu, D. Yan, Z. Li, Z. Ao, M. Zhu, Protrudent iron single-atom accelerated interfacial piezoelectric polarization for self-powered water motion triggered Fenton-like reaction, *Small* 18 (2022) 2105279.
- [27] C. Su, R. Li, C. Li, W. Wang, Piezo-promoted regeneration of Fe²⁺ boosts peroxydisulfate activation by Bi₂Fe₄O₉ nanosheets, *Appl. Catal. B: Environ.* 310 (2022), 121330.
- [28] R.Q. Song, H. Cölfen, Mesocrystals—Ordered nanoparticle superstructures, *Adv. Mater.* 22 (2010) 1301–1330.
- [29] P. Zhang, T. Tachikawa, M. Fujitsuka, T. Majima, The development of functional mesocrystals for energy harvesting, storage, and conversion, *Chem. Eur. J.* 24 (2018) 6295–6307.
- [30] M.H. Liu, Y.H. Tseng, H.F. Greer, W. Zhou, C.Y. Mou, Dipole field guided orientated attachment of nanocrystals to twin-brush ZnO mesocrystals, *Chem. Eur. J.* 18 (2012) 16104–16113.
- [31] A. Shahzad, J. Ali, J. Iftikhar, G.G. Aregay, J. Zhu, Z. Chen, Z. Chen, Non-radical PMS activation by the nanohybrid material with periodic confinement of reduced graphene oxide (rGO) and Cu hydroxides, *J. Hazard. Mater.* 392 (2020), 122316.
- [32] M.-H. Liu, Y.-W. Chen, T.-S. Lin, C.-Y. Mou, Defective mesocrystal ZnO-supported gold catalysts: facilitating CO oxidation via vacancy defects in ZnO, *ACS Catal.* 8 (2018) 6862–6869.
- [33] N.M. Vieno, T. Tuhkanen, L. Kronberg, Seasonal variation in the occurrence of pharmaceuticals in effluents from a sewage treatment plant and in the recipient water, *Environ. Sci. Technol.* 39 (2005) 8220–8226.
- [34] Y. Feng, D. Wu, H. Li, J. Bai, Y. Hu, C. Liao, X.-Y. Li, K. Shih, Activation of persulfates using siderite as a source of ferrous ions: sulfate radical production, stoichiometric efficiency, and implications, *ACS Sustain. Chem. Eng.* 6 (2018) 3624–3631.
- [35] P.K. Klu, M.A.N. Khan, C. Wang, J. Qi, X. Sun, J. Li, Mechanism of peroxymonosulfate activation and the utilization efficiency using hollow (Co, Mn)₃O₄ nanoreactor as an efficient catalyst for degradation of organic pollutants, *Environ. Res.* 207 (2021), 112148.
- [36] L. Fang, K. Liu, F. Li, W. Zeng, Z. Hong, L. Xu, Q. Shi, Y. Ma, New insights into stoichiometric efficiency and synergistic mechanism of persulfate activation by zero-valent bimetal (Iron/Copper) for organic pollutant degradation, *J. Hazard. Mater.* 403 (2021), 123669.
- [37] S. Wang, J. Wang, A novel strategy of successive non-radical and radical process for enhancing the utilization efficiency of persulfate, *Chemosphere* 245 (2020), 125555.
- [38] Y. Zhang, J. Wei, L. Xing, J. Li, M. Xu, G. Pan, J. Li, Superoxide radical mediated persulfate activation by nitrogen doped bimetallic MOF (FeCo/N-MOF) for efficient tetracycline degradation, *Sep. Purif. Technol.* 282 (2021), 120124.
- [39] Y. Wan, J. Wan, Y. Ma, Y. Wang, T. Luo, Sustainable synthesis of modulated Fe-MOFs with enhanced catalyst performance for persulfate to degrade organic pollutants, *Sci. Total Environ.* 701 (2020), 134806.
- [40] G.-E. Yuan, Y. Qin, M. Feng, W. Zhang, X. Ru, X. Zhang, Synergistic activation of persulfate by natural chalcocite and ferrous ions by promoting the cycling of Fe³⁺/Fe²⁺ couple for degradation of organic pollutants, *Ecotoxicol. Environ. Safe* 212 (2021), 111975.
- [41] X. Zhou, C. Luo, M. Luo, Q. Wang, J. Wang, Z. Liao, Z. Chen, Z. Chen, Understanding the synergetic effect from foreign metals in bimetallic oxides for PMS activation: a common strategy to increase the stoichiometric efficiency of oxidants, *Chem. Eng. J.* 381 (2020), 122587.
- [42] J. Lu, Y. Zhou, Y. Zhou, Efficiently activate peroxymonosulfate by Fe₃O₄@MoS₂ for rapid degradation of sulfonamides, *Chem. Eng. J.* 422 (2021), 130126.
- [43] S. Zhu, P. Xiao, X. Wang, Y. Liu, X. Yi, H. Zhou, Efficient peroxymonosulfate (PMS) activation by visible-light-driven formation of polymorphic amorphous manganese oxides, *J. Hazard. Mater.* 427 (2022), 127938.
- [44] M. Liu, H. Qin, H. Xu, Z. Zou, C. Deng, D. Xia, Q. Yu, Y. Zheng, D. Chen, Confine activation peroxymonosulfate by surface oxygen vacancies of BiO_{1-x}Cl to boost its utilization rate, *Sep. Purif. Technol.* (2022), 122711.
- [45] J. Lu, Y. Zhou, L. Ling, Y. Zhou, Enhanced activation of PMS by a novel Fenton-like composite Fe₃O₄/S-WO₃ for rapid chloroxylene degradation, *Chem. Eng. J.* 446 (2022), 137067.
- [46] J. Yang, Y. Huang, Y.-W. Chen, D. Xia, C.-Y. Mou, L. Hu, J. Zeng, C. He, P.K. Wong, H.-Y. Zhu, Active site-directed tandem catalysis on CuO/VO-MnO₂ for efficient and stable catalytic ozonation of S-VOCs under mild condition, *Nano Today* 35 (2020), 100944.
- [47] M. Zhang, X. Lin, Z. Yi, X. Xu, J. Yang, M. Zhu, Enhanced reactive oxidation species generation by ligand-to-metal-charge transfer between oxygen vacancy-rich ZnO mesocrystal with ciprofloxacin pollutants, *Appl. Catal. B: Environ.* 321 (2023), 122033.
- [48] H. Yuan, J. Li, W. Yang, Z. Zhuang, Y. Zhao, L. He, L. Xu, X. Liao, R. Zhu, L. Mai, Oxygen vacancy-determined highly efficient oxygen reduction in NiCo₂O₄/hollow carbon spheres, *ACS Appl. Mater. Inter.* 10 (2018) 16410–16417.
- [49] Y. Liu, C. Ma, Q. Zhang, W. Wang, P. Pan, L. Gu, D. Xu, J. Bao, Z. Dai, 2D electron gas and oxygen vacancy induced high oxygen evolution performances for advanced Co₃O₄/CeO₂ nanohybrids, *Adv. Mater.* 31 (2019) 1900062.
- [50] H. Xiao, W. Zhang, Q. Yao, L. Huang, L. Chen, B. Boury, Z. Chen, Zn-free MOFs like MIL-53(Al) and MIL-125(Ti) for the preparation of defect-rich, ultrafine ZnO nanosheets with high photocatalytic performance, *Appl. Catal. B: Environ.* 244 (2019) 719–731.
- [51] J. Di, J. Xia, M.F. Chisholm, J. Zhong, C. Chen, X. Cao, F. Dong, Z. Chi, H. Chen, Y. X. Weng, Defect-tailoring mediated electron-hole separation in single-unit-cell Bi₂O₃Br nanosheets for boosting photocatalytic hydrogen evolution and nitrogen fixation, *Adv. Mater.* 31 (2019) 1807576.
- [52] S. Gao, B. Gu, X. Jiao, Y. Sun, X. Zu, F. Yang, W. Zhu, C. Wang, Z. Feng, B. Ye, Highly efficient and exceptionally durable CO₂ photoreduction to methanol over freestanding defective single-unit-cell bismuth vanadate layers, *J. Am. Chem. Soc.* 139 (2017) 3438–3445.
- [53] L. Liu, M. Li, F. Chen, H. Huang, Recent advances on single-atom catalysts for CO₂ reduction, *Small Struct.* (2022) 2200188.
- [54] H. Zhang, C. Li, L. Lyu, C. Hu, Surface oxygen vacancy inducing peroxymonosulfate activation through electron donation of pollutants over cobalt-zinc ferrite for water purification, *Appl. Catal. B: Environ.* 270 (2020), 118874.
- [55] H. Li, J. Shang, Z. Yang, W. Shen, Z. Ai, L. Zhang, Oxygen vacancy associated surface Fenton chemistry: surface structure dependent hydroxyl radicals generation and substrate dependent reactivity, *Environ. Sci. Technol.* 51 (2017) 5685–5694.
- [56] X. Hu, Y. Ye, Y. Chen, M. Liu, W. Zhang, M. Zhu, The synergistic interactions of reaction parameters in heterogeneous peroxymonosulfate oxidation: Reaction kinetic and catalytic mechanism, *J. Hazard. Mater.* 421 (2022), 126841.
- [57] W. Tao, X. Yang, Y. Li, R. Zhu, X. Si, B. Pan, B. Xing, Components and persistent free radicals in the volatiles during pyrolysis of lignocellulose biomass, *Environ. Sci. Technol.* 54 (2020) 13274–13281.